

Photoactivities of the visible-light-activated mixed-phase carbon-containing titanium dioxide: The effect of carbon incorporation

Sergey Y. Treschev^a, Po-Wen Chou^a, Yao-Hsuan Tseng^b, Jia-Bin Wang^a,
Elena V. Perevedentseva^a, Chia-Liang Cheng^{a,*}

^a Department of Physics, National Dong Hwa University, Hualien 97401, Taiwan

^b Energy and Environment Research Laboratories, Industrial Technology Research Institute, Hsinchu 31040, Taiwan

Received 26 October 2006; received in revised form 26 September 2007; accepted 28 September 2007

Available online 10 October 2007

Abstract

Photoactivities of the carbon-containing nano-structured titanium dioxide (TiO₂) prepared using a modified sol–gel method as visible-light-responsive photocatalysts were studied. This research aimed to compare four carbon-containing TiO₂ samples, prepared in different conditions, with a commercial nano-structured TiO₂ powders. The prepared titanium dioxide powders were analyzed using Raman spectroscopy and scanning electron microscopy with energy dispersive X-ray spectroscopy. It is found carbon-containing TiO₂ nanoparticles prepared under calcinations at 200 °C exhibited high photocatalytic activity for decoloring of methylene blue and the removal of nitrogen monoxide under both ultraviolet and visible-light illumination. The calcination temperature and incorporated carbons affect the particle size and lattice structure of TiO₂, and hence the photoactivities. The superior photocatalytic effects were attributed to the carbon-containing mixed anatase and rutile phase in the crystal structure of the TiO₂.

© 2007 Elsevier B.V. All rights reserved.

Keywords: Visible-light-activated TiO₂; Carbon-containing TiO₂; Confocal Raman mapping; Photoactivity

1. Introduction

Titanium dioxide (TiO₂) has a wide range of applications in industry and daily life [1–6]. The most interesting aspects of TiO₂ are the properties of photo-induced activities, such as photocatalysis and hydrophilicity properties [6]. TiO₂ has been identified as the most effective and useful photocatalyst. However, practical applications require the photocatalytic effects being activated at visible-light illumination capable to utilize the benefit of sunlight and the low cost of producing that is suitable for industrial scale up production. In general, the key issues for practical photocatalytic applications are the specific surface area, the absorption range of light in solar spectrum and the photoactivity or the efficiency of the photocatalysts. Hence, many new materials and structures are proposed, which can yield more effective reaction under solar radiation [7–9].

To enhance the photocatalytic effect in the visible-light region, many producing methods were proposed including ion-assisted sputtering [10], plasma [11], ion-implantation [12–14], CVD and sol–gel to dope (or incorporate) trace impurity (Cr, W, N, V) in TiO₂ for visible-light-responsive activities [15]. In addition, other materials, such as CdS, TaN₅, TaON and InVO₄, are also used as visible-light-responsive photocatalysts [16,17]. These methods and materials have been usually studied and developed in the field of photocatalytic water splitting. However, for the environmental purification, the cost of photocatalyst must be inexpensive for any practical application. As a result the feasibility of these methods and materials are low for industrial-scale production due to high price, environment-polluted, and instability.

In the present study, a series of carbon-containing, nano-structured titanium dioxide prepared using sol–gel method as visible-light-responsive photocatalysts are studied. In this article, we studied the photocatalytic activities of four carbon-containing TiO₂ samples and compared with a commercial nano-structured TiO₂ powders with focus on the effect of the carbon incorporation on the photoactivities.

* Corresponding author. Tel.: +886 3 863 3696; fax: +886 3 863 3690.

E-mail address: clcheng@mail.ndhu.edu.tw (C.-L. Cheng).

2. Experimental

In this experiment, four different carbon-containing TiO₂ nanoparticle powders were examined and various photocatalytic effects were compared with a commercial nano-structured TiO₂ powder. The first two carbon-containing, nano-structured TiO₂ samples were produced using sol–gel method. In this method, 50 mmol of tetrabutyl orthotitanate (TBOT) was dropped slowly in 90 mL of anhydrous ethanol and 20 mL of deionized water, contained in a 250 mL flask. After complete dissolution, 4 mL of 1 M nitric acid was added to catalyze the hydrolysis and condensation reactions at 25 °C. The mixed solution was uniformly agitated at 500 rpm for 3 h, and then the precipitated titanium hydroxide was produced. After drying at 110 °C, the dried powder was calcinated in air with controlled temperatures for 5 h. The as-prepared carbon-containing TiO₂ powders were subjected to calcinations at temperatures 150 °C (labeled as C150) and 200 °C (labeled as C200), respectively. Details of the samples, the preparation procedures via the sol–gel route under different calcinations temperatures were illustrated in Fig. 1. In our previous study [18], C150 and C200 were found to have satisfactory photocatalytic effects. The second two carbon-containing, nano-structured TiO₂ samples were also synthesis with the same procedures as described above, except cyclohexanol compound was added in this synthesis procedure. The 30 mL of cyclohexanol served as the source of the extra carbon added. The carbonaceous species from TBOT alkoxide groups of titanium salt and cyclohexanol would be doped into or deposited on the TiO₂, as revealed by the results of SEM–EDS and confocal Raman mapping. The as-prepared carbon-containing TiO₂ powders were subjected to calcinations at temperatures 200 °C (labeled as CC6-200) and 500 °C (CC6-500), respectively. One commercially available TiO₂ labeled as UV100 (Sachtleben, Germany) was used for comparison. The UV100 typically has anatase phase with a mean particle size <8 nm and the BET (Brunauer–Emmett–

Teller) surface area 244 m²/g. Methylene blue (MB, C₁₆H₁₈ClN₃S, Koch-Light Laboratory, England) was used without further purification.

UV–vis absorption was analyzed with a powder UV–vis spectrophotometer (UV2450, Shimadzu, Japan). UV and visible-light illumination of TiO₂ photocatalytic decoloring experiments were conducted with solution containing 15 mL (1.6×10^{-5} M) of methylene blue with 5 mg of TiO₂ powder for five different TiO₂ powder samples (UV100, C150, C200, CC6-200 and CC6-500). In each sample, 5 test tubes were prepared for experiments carried out at different time intervals of light illuminations (1, 2, 5, 8, 11 h). The prepared solutions were exposed to the illumination of artificial UV light (F10T8BLB; Sankyo Denki Co., Ltd., Japan) with an intensity of 0.5 mW/cm² and visible light from a regular household incandescent bulb (T55/60W; Philips Lighting, Taiwan) with an intensity of 13.6 mW/cm². The samples were placed in an enclosed dark box, with the light source set at ~10 cm from the samples, at room temperature for the experiment. The emission spectra of UV and visible lamps for decoloring experiments are shown in Fig. 2a and Fig. 2b, respectively. Analytical measurement of methylene blue was carried out with a Jasco V550UV/vis spectrometer (Jasco, Hachioji, Japan) for methylene blue absorbance at the wavelength of 665 nm. The reactant solution of MB was not pre-purged by N₂ or He, so a little amount of O₂ is reasonably present in the decoloring experiment.

The degradation of NO_x was performed in a continuous flow system. The system and the emission spectra of light sources have been reported elsewhere [18]. In this system, the light source was provided using a LED or black lamp, with an intensity of 1 mW/cm². The spectrum of light source was measured using a spectrometer (Ocean Optics, USB2000, USA), based on which the intensity could be calculated. The NO_x degradation was carried out at room temperature using an air stream containing 1.0 ppm NO as feedstock. The NO gas

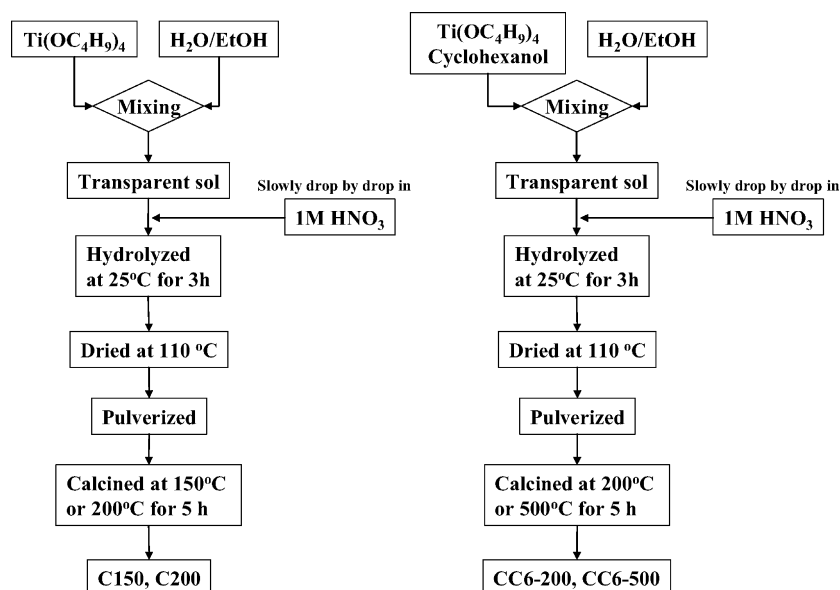


Fig. 1. The procedure of catalysts production by aqueous sol–gel of C150, C200, CC6-200 and CC6-500.

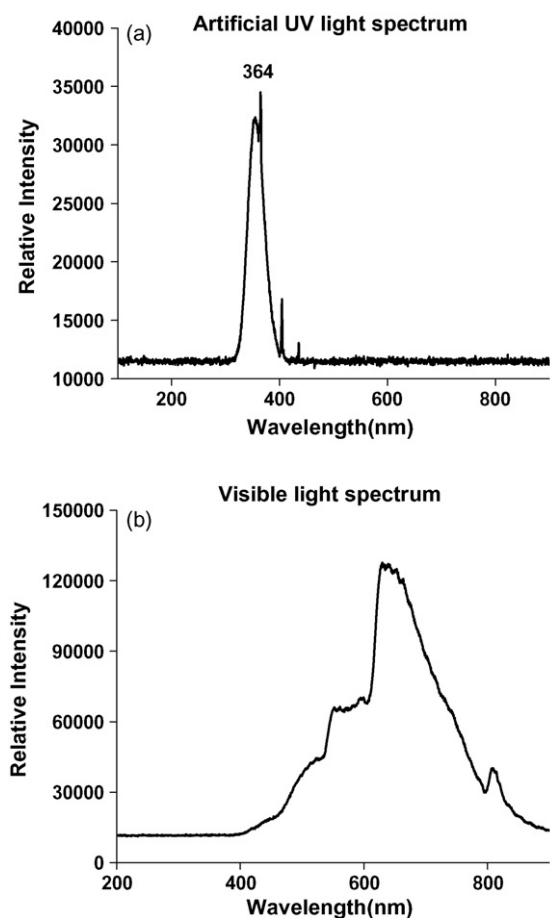


Fig. 2. Spectra of artificial UV light (a) and visible light from table lamp (b) used in this experiment.

was provided from a cylinder containing 100 ppm NO (N_2 balanced, San Fu Chemical, Taiwan) and diluted by a separate air stream. The reaction gas in feeding stream passed through the vessel containing TiO_2 powder (0.5 g) at a flow rate of 1 L/min. For gas phase analysis, the NO and NO_2 concentrations were continuously monitored with an on-line chemiluminescent NO_x analyzer (Eco Physics, CLD 700 AL, Switzerland).

Raman mapping investigation was carried out with a confocal Raman spectrometer (Witec, α -SNOM, Germany) using 488 nm wavelength laser excitation. The surface morphology was studied using scanning electron microscopy (SEM, JEOL JSM6500F, Japan). The SEM is equipped with energy dispersive X-ray spectroscopy (EDS), was used for elemental analysis of the samples.

3. Results and discussion

3.1. UV/vis absorption

There have been reports that the incorporation of carbons in the TiO_2 nanostructure may alter the band gaps, which in turn shifts the absorption to the visible-light range [1,18–21]. In Fig. 3, the functions of the diffuse reflectance spectra of UV100, C150, C200, CC6-200 and CC6-500 are shown. In this figure, the Kubelka–Munk functions, $F(R)$, are used as the equivalent of

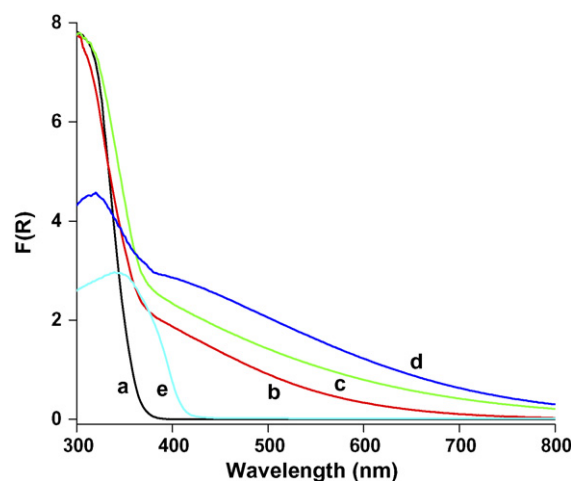


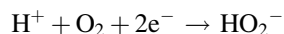
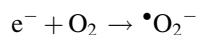
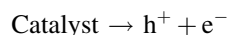
Fig. 3. The function of the diffuse reflectance spectra of UV100 (a), C150 (b), C200 (c), CC6-200 (d) and CC6-500 (e) show red shift of spectra.

absorption. Red shift of spectra to visible-light region for samples C150, C200 and CC6-200 was observed and the absorption tails extended close to 800 nm. The sample CC6-500 has only a little red shift as compared to UV100. UV100 has spectrum corresponding to only UV absorption with wavelength less than 380 nm. The spectra indicate samples C150, C200 and CC6-200 absorb more light in the visible region in comparison to UV100 and CC6-500. In our previous study of the C150 and C200 series [18], we found the calcinations caused the carbon content assisted the amorphous phase to form rutile phase at lower temperature (around 200 °C). On the other hand, high temperature causes desorption of the carbon resulted in only rutile phase. In Fig. 3, we observed that CC6 series also have the same characteristic. This explains why the CC6-500 sample exhibits lower visible-light absorption calcinated at this temperature, since most carbon probably have desorbed as a result of the calcinations. We had also found previously carbon content in the TiO_2 nanostructure might create interface states therefore resulted in narrowing of the band gaps [19]. This effectively lowered the band gap of the as-prepared TiO_2 from 3.2 eV to approximately 2.7 eV, and therefore, resulted in the shifting of the absorption towards the visible-light range for the C200 sample. From Fig. 3, all the carbon-containing TiO_2 samples annealed at lower temperature (less than 200 °C) exhibit shifts of the absorption edges from 380 nm to visible-light range. The observed variation in the absorption tails may depend on the carbon content and the crystal structures in the slightly different carbon-containing TiO_2 nanoparticles. The carbon-containing evidently caused the absorption tails extended to 800 nm region. For CC6-500, possible desorption of carbons might have happened and hence no absorption tail can be observed.

3.2. Photocatalytic activities

The photocatalytic activity of the prepared TiO_2 powders was examined for its decoloring ability on methylene blue upon light illumination with UV or visible lights. Methylene blue (MB) is a heterocyclic aromatic chemical compound with molecular formula $C_{16}H_{18}ClN_3S$. It is widely used as a redox

indicator in analytical chemistry. Solutions of this substance are blue when placed in an oxidizing environment, but will turn colorless if exposed to a reducing agent. For the UV or visible-light photocatalytic degradation over a catalyst, the initiation of this process could be described by the following equations, in which the generated $\bullet\text{O}_2^-$, $\bullet\text{OH}$ and HO_2^- could effectively oxidize the methylene blue [24,25]



After UV and visible-light illumination at various times, the absorption of the methylene blue was checked to represent the decoloring ability of the samples used. We observed decrease of methylene blue absorption peak at 665 nm wavelength region. The changes of absorbance (decoloring ability) of methylene blue for four different samples and one commercial TiO_2 up to 11 h illumination of UV (a) and visible (b) lights are shown in Fig. 4. From Fig. 4, we see the sample C200 has the strongest methylene blue decoloring effect at both UV and visible-light

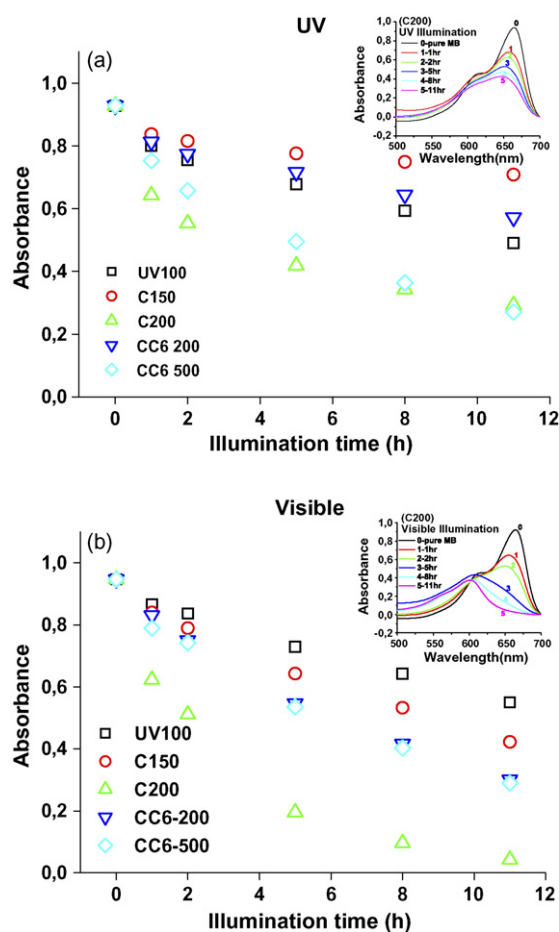


Fig. 4. Summary results of decoloring of the methylene blue after UV (a) and visible light (b) illumination. The absorption spectra of the decoloring of the methylene blue after UV (a) and visible light (b) illumination for sample C200 are shown in the insets of each spectrum.

illuminations. Other sample such as CC6-200 performed modestly. The result suggests sample C200 is more photocatalytic active than other samples in terms of decoloring of methylene blue. Typical absorption spectra of methylene blue at various illumination times are displayed in the insets of Fig. 4 for UV light (Fig. 4a) and visible light (Fig. 4b) for C200 sample. In Fig. 5, the natural logarithm of the concentration ratio of methylene blue before and after illumination was plotted against the illumination time. From this figure, the decoloring reaction on TiO_2 is a first-order reaction and the slope of the straight line is the rate constant (k) of the degradation of methylene blue. Summarized rate constants for both UV and visible-light illumination are depicted in Fig. 6. The samples CC6-500 and C200 have the highest rate constants, 0.107 and 0.094 h^{-1} for UV-light illumination and sample C200 has highest rate constant 0.28 h^{-1} for visible-light illumination, respectively. The rate constants for other samples and the apparent quantum efficiencies are listed in Table 1. Sample UV100 has the lowest rate constant as compared to other samples. The samples CC6-200 and CC6-500 have second highest rate-constant after sample C200 for visible-light illumination. Although the CC6-200 sample has the highest visible absorption, its decoloring ability is lower than the C200 sample. Therefore, the structure of the crystal and the incorporation of carbons may play some role to differentiate the photoactivity of the TiO_2 .

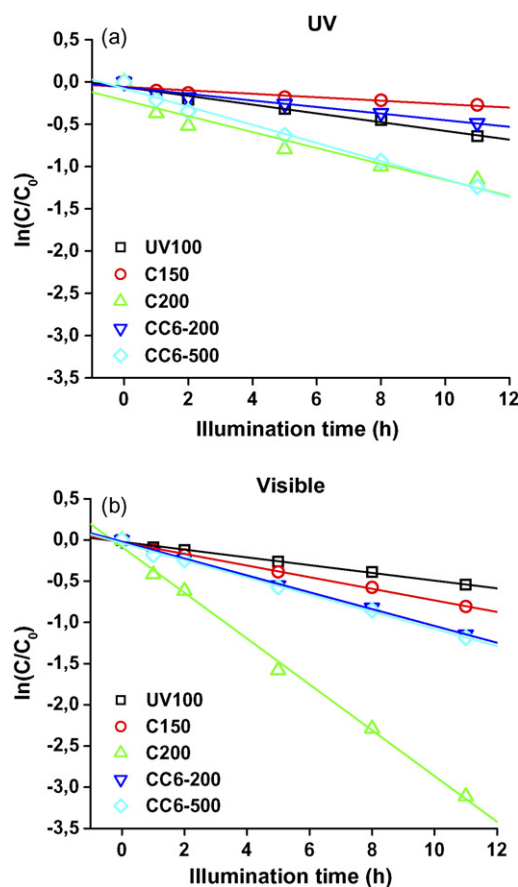


Fig. 5. The natural logarithm of the concentration ratio of the light-induced methylene blue photodegradation before and after UV (a) and visible (b) light illuminations on carbon-containing and commercial UV100 TiO_2 powders.

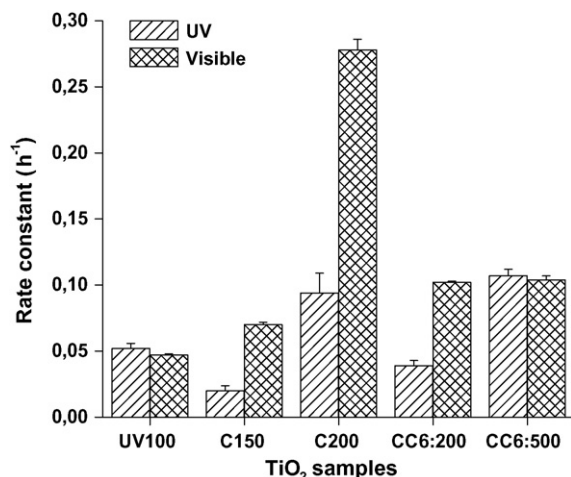


Fig. 6. Diagram of the rate constant after UV and visible illuminations for different TiO₂ powders.

Oxidation of NO is widely used for evaluation of photocatalytic reactivity of TiO₂ powders [3,21–23]. The electron-hole pair (e[−]–h⁺) generated upon light excitation is trapped at the surface of TiO₂ as spatially separated redox active sites. On the surface of TiO₂ irradiated with UV light, the formation of some reactive oxygen species, such as superoxide ion (O₂^{•−}), atomic oxygen (O), O[−], OH and HO₂ radicals, has been reported [24–26]. The general mechanism of NO_x oxidation by photocatalyst has also been discussed [3,21–23]. To illustrate the reaction behavior of photocatalytic oxidation of NO_x, 0.5 g of TiO₂ and 1 mW/cm² of light intensity were used. The oxidation of NO_x under UV and visible light was performed in a continuous flow system [18]. In Fig. 7 the dependence of NO removal rate from different illumination of light emitting diodes (LEDs) for five TiO₂ powder samples is shown. For UV100 and CC6-500 which possesses higher photocatalytic activity in the UV-light region dramatic decrease of NO removal rate was observed from UV to visible-light regions. While for C150, C200 and CC6-200 samples, no significant change was observed in the behavior of NO removal rate except for the red illumination. We observed decrease of NO removal rate for all samples near the red, but in most part of the visible-light region, C200 exhibited the highest NO removing rate. This result agrees well with the absorption

Table 1
Rate constants and quantum efficiencies^a of the photocatalytic activity of five TiO₂ samples

Samples	UV ^b		Visible ^c	
	Rate constant (h ^{−1})	QE × 10 ³	Rate constant (h ^{−1})	QE × 10 ⁵
UV100	0.052 ± 0.005	1.04	0.047 ± 0.001	2.23
C150	0.020 ± 0.004	0.48	0.070 ± 0.002	2.94
C200	0.094 ± 0.015	1.51	0.278 ± 0.008	4.99
CC6-200	0.039 ± 0.004	0.84	0.102 ± 0.001	3.65
CC6-500	0.107 ± 0.005	1.62	0.104 ± 0.003	3.69

Decoloring under UV and visible-light illumination.

^a Quantum efficiency at 11 h of experiment.

^b Apparent main peak of UV illumination at 365 nm.

^c Apparent main peak of visible-light illumination at 580 nm.

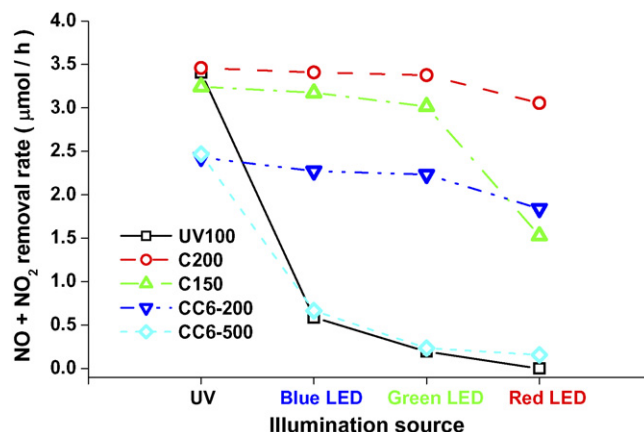


Fig. 7. Dependence of NO removal rate on illumination by different LEDs for five TiO₂ powder samples; catalyst loading: 0.5 g, intensity of irradiation: 1 mW/cm², relative humidity: 55%, inlet concentration of NO: 1 ppm, inlet flow rate: 1 L/min, reaction temperature: 27 °C and operation time: 0.5 h.

spectra observed in Fig. 3. The apparent quantum efficiency (Φ_a) was computed based on the following equations [27] are listed in Table 2.

$$\Phi_a (\text{decoloring}) = \frac{\text{mole of MB degraded}}{\text{Einstein of incident photons}},$$

and

$$\Phi_a (\text{NO}_x\text{-removal}) = \frac{\text{mole of (NO + NO}_2\text{) degraded}}{\text{Einstein of incident photons}}.$$

The quantum efficiencies of photodegradation of NO_x reaction were larger than that of photocatalytic decoloring reaction. The reason for this phenomenon is the mass transfer resistance of gas–solid interface (NO_{x(g)}–TiO_{2(s)}) is much smaller than that of liquid–solid interface (MB_(l)–TiO_{2(s)}).

3.3. Crystalline structure

The differences in photocatalytic activities observed under visible-light illumination between commercial sample UV100 and the prepared samples with carbon-containing C150, C200, CC6-500 and CC6-200 samples can be explained by the

Table 2
Degradation of NO_x and quantum efficiencies^a of five samples under UV and visible-light illumination

Samples	QE × 10 ³			
	UV ^b	BLED ^c	GLED ^d	RLED ^e
UV100	6.21	0.82	0.25	0
C150	5.91	4.48	3.87	1.60
C200	6.30	4.81	4.34	3.2
CC6-200	4.42	3.20	2.87	1.93
CC6-500	4.50	0.94	0.30	0.16

^a Quantum efficiency at 30 min of experiment.

^b Apparent main peak of UV illumination at 365 nm.

^c Apparent main peak of blue LED illumination at 470 nm.

^d Apparent main peak of visible-light illumination at 520 nm.

^e Apparent main peak of visible-light illumination at 635 nm.

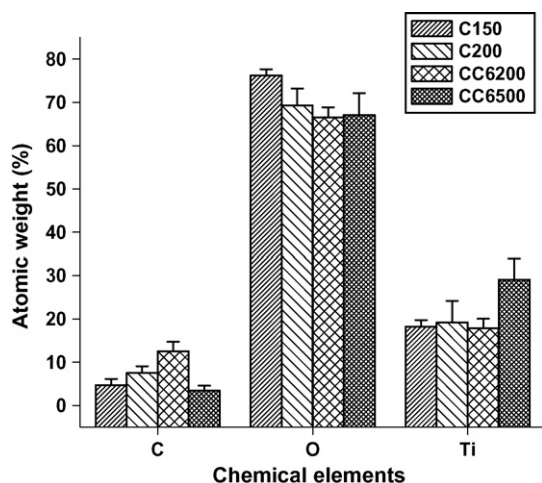


Fig. 8. Chemical elements contents in different TiO₂ powders.

differences in lattice structures and surface properties. It is well known that commercial UV100 TiO₂ powder has only anatase phase with a band gap of 3.2 eV [28]. This band gap absorbs in the UV range with wavelength less than 380 nm where photocatalytic activity can be observed; whereas the prepared carbon-containing TiO₂ powders have different lattice structures in contrast to the UV100. In our previous study, mixed-phase of lattice structures was observed by confocal Raman spectroscopy and transmission electron microscopy (TEM) in the examined TiO₂ powders [18,19]. From Figs. 3–5 different photocatalytic activities were observed for these samples.

In an effort to understand the structural differences, which result in different photocatalytic activities of the samples, we

carried out experiments using scanning electron microscopy with energy dispersive X-ray spectroscopy (SEM-EDS) and confocal Raman microscopy. SEM-EDS experiments allow accessing the relative mean quantity of containing elements in TiO₂ powder after different calcinations temperatures. The elemental analysis results are presented in Fig. 8. Atomic weight for the containing chemical elements does not vary appreciably. Although CC6-500 sample had more carbon before annealing procedure in comparison with C150 and C200 samples, higher temperature (500 °C) caused the evaporation of most carbons. This is not observed for CC6-200 sample, which may have carbons initially as CC6-500 sample but as it is subjected to lower temperature calcinations, its carbon content does not change much. This result suggests carbon containing is important in enhancing the photocatalytic effects. The slightly different carbon quantity, in addition to the crystal structures, further indicates the carbon quantity can play important role in the photocatalytic effect. However, in this experiment, quantitative results cannot be obtained.

3.4. Confocal Raman mapping

To understand better the structure of the examined samples and the role of the carbons, confocal Raman spectral mapping of carbon-containing samples C150, C200, CC6-200 and CC6-500 was taken from different areas of samples and the results are depicted in Figs. 9–12. These figures consist of two parts. One part shows images of the Raman intensity distribution of the scanned 10 μm × 10 μm region on the samples. The second part of the figure presents the Raman spectra taken from different marked points of the sample. The bright part of the images

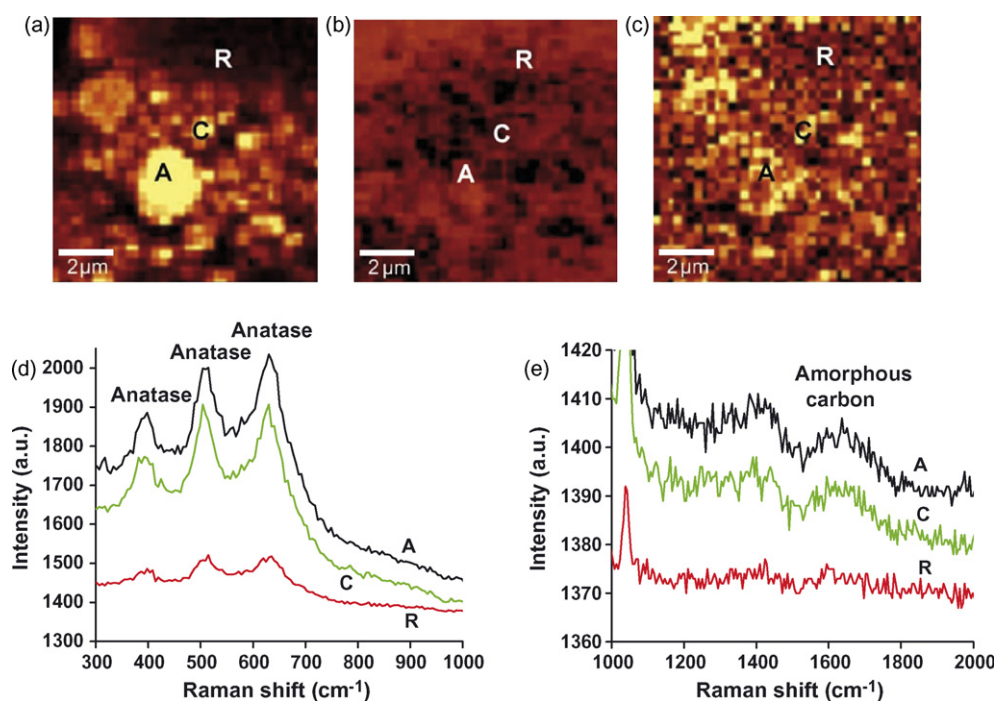


Fig. 9. Confocal Raman mapping (a–c) and Raman spectra (d and e) of sample C150 taken at different points of samples. A: anatase phase of TiO₂, R: rutile phase of TiO₂ and C: carbon species. The bright color in (a), (b) and (c) indicate anatase, rutile and carbon phases, respectively. (For interpretation of the references to color in this figure legend, the reader is referred to the web version of the article.)

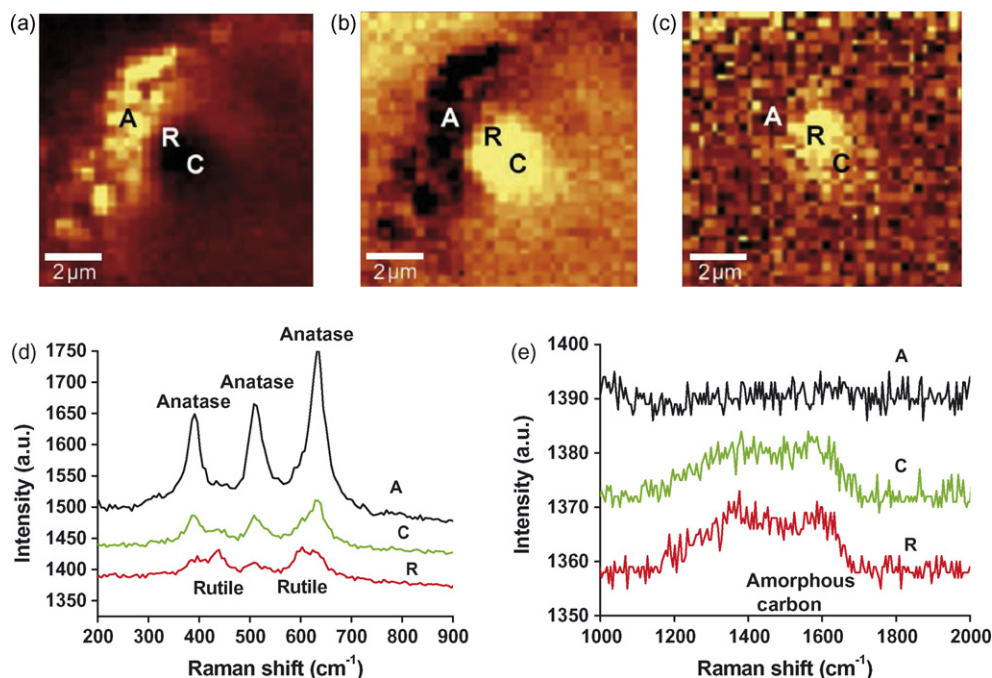


Fig. 10. Confocal Raman mapping (a–c) and Raman spectra (d and e) of sample C200 taken at different points of sample. A: anatase phase of TiO_2 , R: rutile phase of TiO_2 and C: carbon species. The bright color in (a), (b) and (c) indicate anatase, rutile and carbon phases, respectively. (For interpretation of the references to color in this figure legend, the reader is referred to the web version of the article.)

display the locked Raman shifts intensities; for anatase phase (labeled as A, Fig. 9–12, a): $586\text{--}682\text{ cm}^{-1}$; for rutile phase (labeled as R, Fig. 9–12, b): $421\text{--}461\text{ cm}^{-1}$; for amorphous carbon (labeled as C, Fig. 9–12, c): $1556\text{--}1675\text{ cm}^{-1}$. The corresponding Raman spectra for various structures of TiO_2 differ when trace of carbon structures are observed. For

convenience Raman spectra were divided into two parts; from 300 to 1000 cm^{-1} for the TiO_2 (Figs. 9–12d) and from 1000 to 2000 cm^{-1} for the carbon structures (Figs. 9–12e). Three most visible peaks in these figures are around 390 , 510 and 630 cm^{-1} , assigned to anatase phase (A); two peaks around 325 and 360 cm^{-1} are from brookite phase (B); two peaks around 430 and

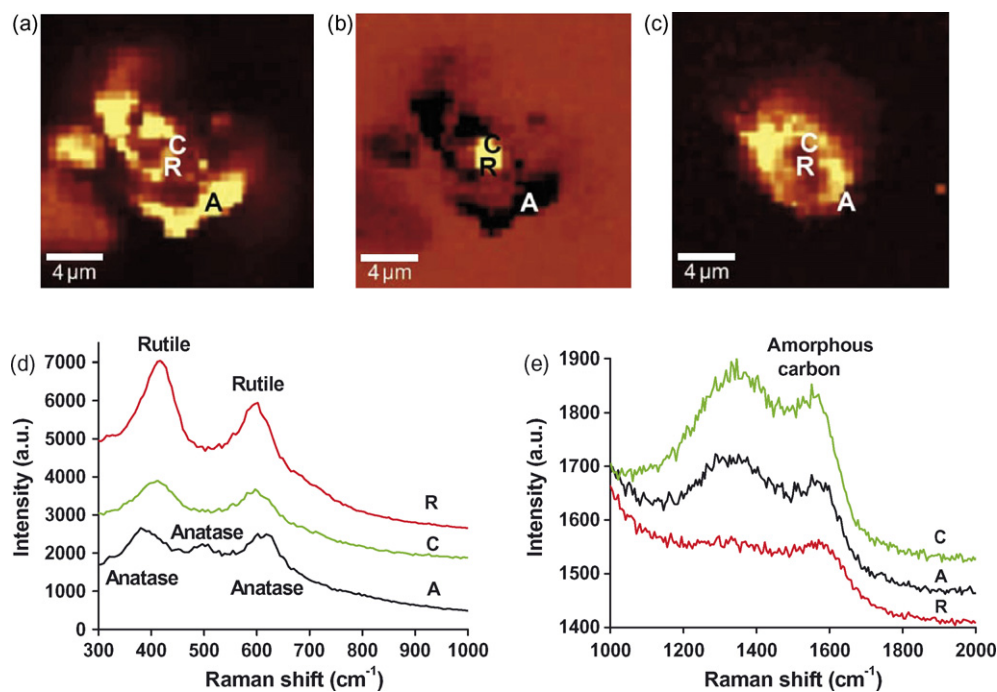


Fig. 11. Confocal Raman mapping (a–c) and Raman spectra (d and e) of sample CC6-200 taken at different points of sample. A: anatase phase of TiO_2 , R: rutile phase of TiO_2 and C: carbon species. The bright color in (a), (b) and (c) indicate anatase, rutile and carbon phases, respectively. (For interpretation of the references to color in this figure legend, the reader is referred to the web version of the article.)

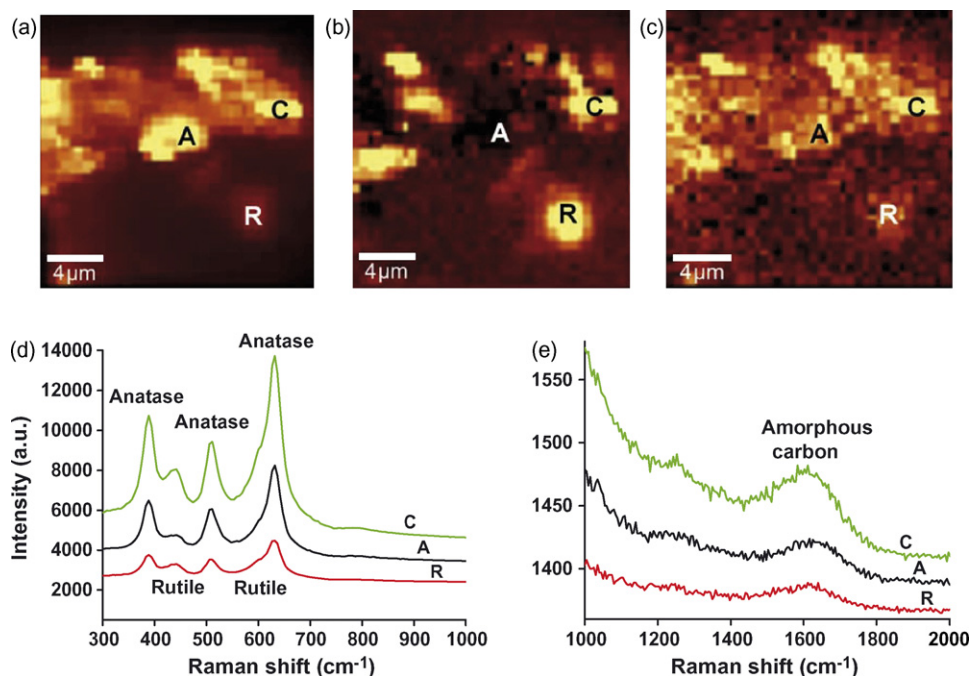


Fig. 12. Confocal Raman mapping (a–c) and Raman spectra (d and e) of sample CC6-500 taken at different points of samples. A: anatase phase of TiO_2 , R: rutile phase of TiO_2 and C: carbon species. The bright color in (a), (b) and (c) indicate anatase, rutile and carbon phases, respectively. (For interpretation of the references to color in this figure legend, the reader is referred to the web version of the article.)

605 cm^{-1} are for the rutile phase (R). In addition, low intensity peaks on 1600 cm^{-1} are from amorphous carbon (C). All samples have apparent peaks of anatase phase. The sample UV100 has uniform anatase phase which corresponds to three anatase peaks in Raman spectra (not shown here). Others samples have brookite and rutile phase beside anatase phase. Different samples, C200, C150, CC6-200 and CC6-500, consist of distinct ratio of anatase and rutile phases. The sample CC6-500 in all points has both anatase and rutile phases (Fig. 12d). It is possible that the rutile phase arises from phase transformation directly from the anatase crystals at the 500°C calcinations. At this temperature, the carbon in the vicinity of the observed rutile structure may have already been desorbed from the surface of the particles. Unlike C200 (Fig. 10d) and CC6-200 (Fig. 11d) samples, where anatase and rutile phases have been randomly mixed in the crystalline, and carbon can always be observed near the rutile structures. It is presumable that the rutile phase in the mixed phases has been phase transformed directly from amorphous TiO_2 as the usual anatase to rutile phase transformation happens at temperature higher than 600°C , and the phase transformation is assisted by the containing carbons at lower temperature. After the phase transformation, the carbon remains in close contact with the rutile structures. This is evident from the co-existing of the rutile phase and carbon structures observed in the Raman mapping (Fig. 10a–c). Therefore, in terms of Raman signals, the C200 and CC6-200 have the similar crystal structure; i.e. the anatase and the rutile phases are mixed where rutile phase is covered with carbon structures, and randomly distributed. While the C150 and CC6-500 behave differently. For the C150 (Fig. 9d), the calcinations temperature was not high enough to cause the amorphous TiO_2 to transform to rutile phase. As to CC6-500, the temperature was

high enough for desorption of the carbon and resulted in uniformly distributed anatase and rutile phases and less carbon. The carbon between the mixed phases plays important roles in the narrowing of the band gap and visible-light absorption of the TiO_2 samples. More importantly, it may be responsible for the enhanced photoactivity. In our last investigation, carbons contained in the mixed phases of TiO_2 effectively lower the band gap by introducing interface states [19]. This is also evidently seen in this experiment. As shown in Fig. 3, the absorption curve of the sample CC6-500 has the same shape with the sample UV100. The curve CC6-500 has shifted to red region in comparison with the sample UV100, this indicates the narrowing of band gap of sample CC6-500 perhaps due to the mixed phases, but with few carbons in the mixed-phase region. The curves for samples C200, C150 and CC6-200 have different shapes than the curve for sample UV100, and have two parts. First part, like for sample UV100, corresponds to narrowing band gap that shifts to the red region. The second part of curve consists of long tail extended to 800 nm . This part is attributed to carbon species-covered and/or defected titania powders that introduced interface states between the band gaps [19]. Temperature 150°C is not high enough for transformation anatase to rutile phases even with the carbon existing. This is consistent with our Raman observation and assumption. The main difference between samples C200 and CC6-200 is in the carbon containing. These samples have the same calcination temperature but difference ratio between anatase and rutile phase. We assume carbon assists the transformation from amorphous phases to rutile phase can happen at this temperature, but the amount of carbons and the positions of the carbons are important. The carbon assists only the amorphous TiO_2 in phase transform to rutile phase and may serve as traps for the photo-activated electron–hole pairs. In four

different samples, C200 has the optimal condition of preparation and has better balance between TiO_2 phases resulting in the superior photocatalytic activity in visible-light activation of the sample investigated.

4. Conclusions

We have investigated the photocatalytic effects of visible-light-activated nano-structured TiO_2 powders prepared using a modified sol–gel method. The photocatalytic activity was compared with a commercial UV activated TiO_2 powders for its decoloring ability of methylene blue and NO oxidation rates on these samples. The most photocatalytic active sample after illumination of UV and visible light is sample C200. As well we found that sample C200 is more photocatalytic active after illumination of visible light in comparison with UV light. The sample C200 has optimal balance between TiO_2 phases for better photocatalytic activity activated by visible light. SEM–EDS, confocal Raman mapping and Raman spectroscopic experiments showed distinct structures and the effect of carbon containing on the photocatalytic properties of different TiO_2 samples. The carbon assists the phase transformation of the amorphous phase TiO_2 directly to rutile phase, creates interface between the anatase and carbon covering rutile phase. The band gap was lowered due to the interface states in the mixed phase, and the photoactivities were enhanced due to carbon covering which may effectively serve as traps for the created electron and hole pairs and result in optimal photoactivities.

Acknowledgement

The authors want to express thanks to the National Science Council of Taiwan, Republic of China for financial supporting this research under contract No. NSC-95-2120-M-259-003.

References

- [1] M. Kaneko, I. Okura (Eds.), *Photocatalysis: Science and Technology*, Springer-Verlag, Japan, 2002.
- [2] A. Fujishima, K. Honda, *Nature* 238 (1972) 37–38.
- [3] T. Ibusuki, K. Takeuchi, *J. Mol. Catal.* 88 (1994) 93–102.
- [4] M.R. Hoffmann, S.T. Martin, W. Choi, D.W. Bahnemann, *Chem. Rev.* 95 (1995) 69–96.
- [5] O. Khaselev, J.A. Turner, *Science* 280 (1998) 425–427.
- [6] A. Fujishima, T.N. Rao, D.A. Tryk, *J. Photochem. Photobiol. C: Photochem. Rev.* 1 (2000) 1–21.
- [7] J. Yoshimura, Y. Ebina, J. Kondo, K. Domen, A. Tanaka, *J. Phys. Chem.* 97 (1993) 1970–1973.
- [8] A. Kudo, I. Mikami, *Chem. Lett.* 27 (1998) 1027–1028.
- [9] Z. Zou, J. Ye, K. Sayama, H. Arakawa, *Nature* 414 (2001) 625–627.
- [10] R. Asahi, T. Morikawa, T. Ohwaki, K. Aoki, Y. Taga, *Science* 293 (2001) 269–271.
- [11] I. Nakamura, N. Negishi, S. Kutsuna, T. Ihara, S. Sugihara, K. Takeuchi, *J. Mol. Catal. A: Chem.* 161 (2000) 205–212.
- [12] H. Yamashita, M. Harada, J. Misaka, M. Takeuchi, K. Ikeue, M. Anpo, *J. Photochem. Photobiol. A: Chem.* 148 (2002) 257–261.
- [13] M. Anpo, M. Takeuchi, K. Ikeue, S. Dohshi, *Curr. Opin. Solid State Mater. Sci.* 6 (2002) 381–388.
- [14] T.-S. Yang, M.-C. Yang, C.-B. Shiu, W.-K. Chang, M.S. Wong, *Appl. Surf. Sci.* 252 (2006) 3729–3736.
- [15] K. Rajeshwar, C.R. Chenthamarakshan, S. Goeringer, M. Djukic, *Pure Appl. Chem.* 73 (2001) 1849–1860.
- [16] G. Hitoki, A. Ishikawa, T. Takata, J.N. Kondo, M. Hara, K. Domen, *Chem. Lett.* 31 (2002) 736–737.
- [17] G. Hitoki, T. Takata, J.N. Kondo, M. Hara, H. Kobayashi, K. Domen, *Chem. Commun.* 16 (2002) 1698–1699.
- [18] Y.-H. Tseng, C.-S. Kuo, C.-H. Huang, Y.-Y. Li, P.-W. Chou, C.-L. Cheng, M.S. Wong, *Nanotechnology* 17 (2006) 2490–2497.
- [19] P.W. Chou, S. Treschev, P.-H. Chung, C.-L. Cheng, Y.-H. Tseng, Y.-J. Chen, M.S. Wong, *Appl. Phys. Lett.* 89 (2006) 131919(1)–131919(3).
- [20] L. Lin, W. Lin, Y.X. Zhu, B.Y. Zhao, Y.C. Xie, Y. He, Y.F. Zhu, *J. Mol. Catal. A: Chem.* 236 (2005) 46–53.
- [21] T. Sano, N. Negishi, K. Koike, K. Takeuchi, S. Matsuzawa, *J. Mater. Chem.* 14 (2004) 380–384.
- [22] N. Negishi, K. Takeuchi, T. Ibusuki, *J. Mater. Sci.* 33 (1998) 5789–5794.
- [23] S. Matsuda, H. Hatano, A. Tsutsumi, *Chem. Eng. J.* 82 (2001) 183–188.
- [24] A. Walker, M. Formenti, P. Meriaudeau, S.J. Teichner, *J. Catal.* 50 (1977) 237–243.
- [25] W. Behnke, F. Nolting, C. Zetzsch, *J. Aerosol. Sci.* 18 (1987) 65–71.
- [26] C.-S. Kuo, Y.-H. Tseng, C.-H. Huang, Y.-Y. Li, *J. Mol. Catal. A* 270 (2007) 93–100.
- [27] I. Oja, A. Mere, M. Krunk, C.H. Solterbeck, M. Es-Souni, *Solid State Phenom.* 99/100 (2004) 259–262.
- [28] A.L. Linsebigler, G. Lu, J.T. Yates, *Chem. Rev.* 95 (1995) 735–758.